Bulletin of the Seismological Society of America, Vol. 101, No. 5, pp. 2308–2322, October 2011, doi: 10.1785/0120100076

Earthquake Ruptures with Strongly Rate-Weakening Friction and Off-Fault Plasticity, Part 2: Nonplanar Faults

by Eric M. Dunham, David Belanger, Lin Cong, and Jeremy E. Kozdon

Abstract Observations demonstrate that faults are fractal surfaces with deviations from planarity at all scales. We study dynamic rupture propagation on self-similar faults having root mean square (rms) height fluctuations of order 10^{-3} to 10^{-2} times the profile length. Our 2D plane strain models feature strongly rate-weakening fault friction and off-fault Drucker–Prager viscoplasticity. The latter bounds otherwise unreasonably large stress concentrations in the vicinity of bends. Our choice of a cohesionless yield function prevents tensile stress states and thus fault opening. A consequence of strongly rate-weakening friction is the existence of a critical background stress level above which self-sustaining rupture propagation, in the form of self-healing slip pulses, first becomes possible. Around this level, at which natural faults are expected to operate, ruptures become extremely sensitive to fault roughness and exhibit substantial fluctuations in rupture velocity. Except for shallow inclinations of the maximum compressive stress to the fault (less than about 20°), the fluctuations are anticorrelated with the local fault slope. These accelerations and decelerations of the rupture, together with naturally emerging slip heterogeneity, excite waves of all wavelengths and result in ground acceleration spectra that are flat at high frequency, consistent with observed strong motion records.

Introduction

Natural fault surfaces exhibit slight deviations from planarity at all scales (Brown and Scholz, 1985; Power and Tullis, 1988, 1991, 1995; Lee and Bruhn, 1996; Renard *et al.*, 2006; Sagy *et al.*, 2007; Candela *et al.*, 2009; Resor and Meer, 2009; Kaven and Pollard, unpublished manuscript, 2011). Slip on such faults perturbs the local stress field, leading to inelastic deformation of the off-fault material and increasing the resistance to slip (Chester and Chester, 2000). Roughness-induced stress perturbations will alter rupture propagation, both by introducing heterogeneities in the slip distribution and by causing rapid accelerations and decelerations of the rupture front. These processes generate high-frequency seismic waves (Haskell, 1964; Madariaga, 1977; Boore and Joyner, 1978; Spudich and Frazer, 1984).

In this work, we explore how fault roughness influences the spontaneous propagation of shear ruptures using 2D plane strain models. We use strongly rate-weakening fault friction, as supported by many recent laboratory experiments (Tsutsumi and Shimamoto, 1997; Tullis and Goldsby, 2003a, 2003b; Prakash and Yuan, 2004; Di Toro *et al.*, 2004; Hirose and Shimamoto, 2005; Beeler *et al.*, 2008) and account for off-fault inelastic deformation in the framework of continuum plasticity (Andrews, 2005; Ben-Zion and Shi, 2005; Duan and Day, 2008; Templeton and Rice, 2008; Viesca *et al.*, 2008; Ma and Beroza, 2008). The latter prevents unreasonably large stress concentrations around abrupt bends in the fault, particularly large tensile stresses that would promote fault opening. At least for the particular elastic-plastic model we use, off-fault plasticity completely eliminates fault opening. This study is the second of a two-part series. The first part (Dunham *et al.*, 2011, hereinafter referred to as Part 1), investigates rupture dynamics with plasticity and strongly rate-weakening friction laws on flat faults. The present study extends this to nonplanar faults.

Our focus is entirely on roughness at scales larger than the maximum slip in a single event. Of course, roughness exists at scales less than the slip as well, but that particular limit is presently inaccessible to us, at least in direct computational simulations of rupture propagation along entire faults. Despite this approximation, our models account for fault roughness over three orders of magnitude in scale. While our results can be presented in nondimensional form, we can also view our simulations as representing earthquakes on faults of ~100 km length, with roughness down to ~100 m (the numerical grid spacing is yet another order of magnitude smaller than this to ensure proper resolution).

Perturbations to the rupture at these shortest wavelengths excite waves at frequencies up to ~10 Hz. The high-frequency band between ~1 and 10 Hz is of particular interest to earthquake engineers, as the fundamental frequency of most man-made structures (with notable exceptions such as tall buildings) lies within it.

Studies of strong motion accelerograms indicate a loss of coherence at high frequencies (Housner, 1947). Indeed, the portion of far-field acceleration records corresponding to direct shear-wave arrivals are, to a first approximation, bandlimited white noise (Hanks, 1979; McGuire and Hanks, 1980; Hanks and McGuire, 1981). While local site effects and scattering along the path certainly contribute to high-frequency ground motion, observations suggest that the source process itself becomes random at short wavelengths and that fluctuations in slip and rupture velocity assume a stochastic character. This idea has formed the basis of a wide variety of ground motion and earthquake source models.

In the most direct approach, synthetic acceleration records are generated as (nonstationary) stochastic time series (e.g., Housner, 1955; Iyengar and Iyengar, 1969; Boore, 1983). Others have developed stochastic source models. Many such approaches are kinematic in nature and either impose a fractal distribution of slip heterogeneity or build a composite source model from a fractal distribution of small events (e.g., Andrews, 1980, 1981; Papageorgiou and Aki, 1983; Herrero and Bernard, 1994; Zeng *et al.*, 1994). Such models are widely used to generate synthetic broadband seismograms (e.g., Saikia and Somerville, 1997; Hartzell *et al.*, 1999; Pitarka *et al.*, 2000; Mai and Beroza, 2003). A review of these and other models is given by Boore (2003). A related approach is taken in stochastic dynamic models, in which heterogeneity is added to the initial stress distribution or friction law parameters on flat faults (e.g., Andrews, 1980, 1981; Oglesby and Day, 2002; Guatteri *et al.*, 2003; Ripperger *et al.*, 2007). Many of these works suggest that the imposed heterogeneities should be regarded as a proxy for unmodeled geometric complexities. As Andrews (1980) states in his pioneering study, "Variation of sliding friction on a plane is intended to represent the effect of random geometric irregularity of the fault surface."

In the present work, we directly account for geometric irregularities and the associated set of physical processes that are likely to be active during coseismic slip on rough surfaces. Our models suggest how the random properties of natural fault surfaces might be connected to the observed levels and character of high-frequency ground motion (though a direct comparison with data is limited by the 2D nature of our simulations). As such, our eventual aim is to use this type of model to explore the transition between coherent low-frequency ground motion and random high-frequency ground motion, which remains poorly understood despite its importance in the generation of synthetic broadband seismograms for seismic hazard calculations.

Field and Laboratory Measurements of Fault Roughness

Fault surface roughness can be quantified in a variety of ways (e.g., Russ, 1994; Candela *et al.*, 2009). Consider a 1D profile of the form

$$y = h(x). \tag{1}$$

One of the simplest quantities that can be determined is the root mean square (rms) roughness. For a profile measured over length L (and that, consequently, includes all wavelengths of roughness, λ, less than L), this is defined as

$$h_{\mathrm{rms}}(\lambda < L) = \sqrt{\frac{1}{L}\int_{-L/2}^{L/2} h^2(x)dx}. \tag{2}$$

As revealed in the original studies by Brown and Scholz (1985), Aviles *et al.* (1987), Okubo and Aki (1987), Power and Tullis (1988, 1991, 1995), and Lee and Bruhn (1996), the rms roughness is not an intrinsic property of the fault surface but instead depends on the profile length L. This is a well-known property of fractal surfaces (e.g., Russ, 1994). The early studies concluded that natural fault surfaces are self-similar fractals; that is, they are statistically identical when viewed at different scales. An example is shown in Figure 1.

To be more precise, we assume that $h(x)$ is a stationary Gaussian random function with zero mean. That is, $E[h] = 0$, where $E[\cdot]$ denotes an ensemble average or expectation value that can be calculated as

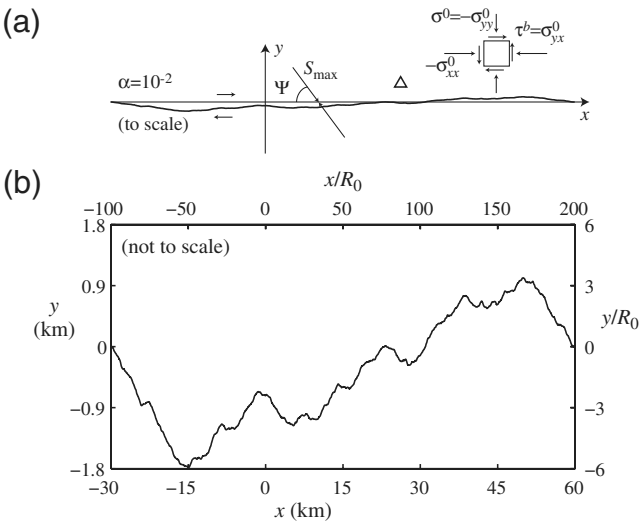

Figure 1. Bandlimited self-similar fault profile, $y = h(x)$, with amplitude-to-wavelength ratio $\alpha = 10^{-2}$, (a) shown to scale, and (b) exaggerated in the y direction to emphasize fluctuations. Synthetic seismograms are calculated at station marked with triangle in (a). The maximum principal stress, $S_{\max}$, is inclined at angle Ψ to $y = 0$. Fault strength drops over a distance of $\sim R_0$; $R_0 =$ 300 m is used in dimensional scales. Roughness is present at wavelengths $\lambda \geq \lambda_{\min} = 1.25R_0$ (= 375 m) in this example.

$$E[h] = \int_{-\infty}^{\infty} h p(h) dh, \tag{3}$$

where $p(h)$ is the probability density function characterizing the profile. We take $p(h)$ to be Gaussian, though to the best of our knowledge there are no reports in the literature concerning the one-point statistics of natural fault surfaces. We further assume that the two-point autocorrelation function of h depends only on the relative separation of the two points: $R_h(x) = E[h(\xi)h(\xi + x)]$. Assuming ergodicity of the fault profile, the ensemble average can be replaced with a spatial average over a single realization of the profile:

$$R_h(x) = \lim_{L\to\infty} \frac{1}{L} \int_{-L/2}^{L/2} h(\xi)h(\xi + x) d\xi. \tag{4}$$

The power spectral density is the Fourier transform of the autocorrelation function

$$P_h(k) = \int_{-\infty}^{\infty} R_h(x) e^{-ikx} dx. \tag{5}$$

Note that $P_h(k)$ is defined for both positive and negative k (it is the two-sided spectral density). Measurements suggest a power law expression for the spectral density,

$$P_h(k) = C_h |k|^{-\beta}, \tag{6}$$

with $1 < \beta \leq 3$. For such fractal profiles, the rms roughness, which would typically be defined as $h_{\text{rms}} = \sqrt{E[h^2]}$, where

$$E[h^2] = R_h(0) = \frac{1}{2\pi} \int_{-\infty}^{\infty} P_h(k) dk, \tag{7}$$

is infinite. [The second equality in equation (7) follows from the inverse Fourier transform of equation (5)]. Thus, we define the bandlimited rms roughness between wavenumbers k_{min} and k_{max} as

$$h_{\text{rms}}(k_{\text{min}}, k_{\text{max}}) = \sqrt{\frac{1}{\pi} \int_{k_{\text{min}}}^{k_{\text{max}}} P_h(k) dk}, \tag{8}$$

in which we have accounted for the contributions from negative k by doubling the contributions from the corresponding positive k (because $P_h(k)$ is even in k).

To facilitate comparison with other studies in the literature, we also define the one-sided spectral density, $S_h(\kappa)$, as a function of the inverse wavelength $\kappa = 1/\lambda = k/2\pi$. The rms roughness between inverse wavelengths $\kappa_{\text{min}} = k_{\text{min}}/2\pi = 1/\lambda_{\text{max}}$ and $\kappa_{\text{max}} = k_{\text{max}}/2\pi = 1/\lambda_{\text{min}}$ is

$$h_{\text{rms}}(k_{\text{min}}, k_{\text{max}}) = \sqrt{\int_{\kappa_{\text{min}}}^{\kappa_{\text{max}}} S_h(\kappa) d\kappa}. \tag{9}$$

Comparison of the two expressions for $h_{\text{rms}}(k_{\text{min}}, k_{\text{max}})$ shows that $S_h(\kappa) = 2P_h(k = 2\pi\kappa)$.

For the power law spectral density in equation (6),

$$h^2_{\text{rms}}(k_{\text{min}}, k_{\text{max}}) = \frac{C_h}{\pi(\beta - 1)} (k_{\text{min}}^{-\beta+1} - k_{\text{max}}^{-\beta+1}). \tag{10}$$

The rms roughness is dominated by the longest wavelengths; this is evident if we set $k_{\text{min}} = 2\pi/L$ and take $k_{\text{max}} \to \infty$:

$$h^2_{\text{rms}}(2\pi/L, \infty) = \frac{C_h}{\pi(\beta - 1)} \left(\frac{L}{2\pi}\right)^{\beta-1}. \tag{11}$$

In the particular case of $\beta = 3$, the rms roughness is proportional to the profile length L:

$$h_{\text{rms}}(2\pi/L, \infty) = \sqrt{\frac{C_h}{(2\pi)^3}} L = \alpha L, \tag{12}$$

which serves to define the amplitude-to-wavelength ratio $\alpha = \sqrt{C_h/(2\pi)^3}$. Such a profile, having spectral density $P_h(k) = (2\pi)^3\alpha^2|k|^{-3}$ or $S_h(\kappa) = 2\alpha^2|\kappa|^{-3}$, is known as self-similar.

Fluctuations in the slope of the fault profile,

$$m(x) = dh/dx, \tag{13}$$

have an autocorrelation function $R_m(x) = -d^2R_h(x)/dx^2$ and spectral density $P_m(k) = k^2P_h(k)$. For a self-similar fault,

$$P_m(k) = (2\pi)^3\alpha^2|k|^{-1}, \tag{14}$$

such that the bandlimited rms fault slope is

$$m_{\text{rms}}(k_{\text{min}}, k_{\text{max}}) = 2\pi\alpha\sqrt{2\ln(k_{\text{max}}/k_{\text{min}})}. \tag{15}$$

Neither the shortest nor the longest wavelengths dominate the rms slope; divergence in the rms slope can occur either by decreasing the minimum wavelength to zero or by increasing the maximum wavelength to infinity.

Measurements indicate that faults have larger α in the direction perpendicular to slip than in the slip-parallel direction. Values of $\alpha = 10^{-2}$ are typical for the slip-perpendicular direction, while values of α between 10^{-3} and 10^{-2} characterize the slip-parallel direction; the smaller end of this range is more representative of mature faults (Power and Tullis, 1991). Sagy and Brodsky (2009) have suggested that as faults mature, the wear processes that accompany slip decrease α. It should be noted, however, that measurements of $\alpha = 10^{-3}$ for mature faults quantify the roughness of single fault strands; many fault zones contain multiple strands or segments, in some cases anastamosing; taken as a whole, the combination of structures that accommodate displacement in an earthquake might be more accurately described by a larger value of α. For example, Chester *et al.* (2004) find that while the prominent fracture surface of the Punchbowl fault in California (which likely accommodated

the majority of ~44 km relative displacement) has $\alpha \approx 10^{-3}$, the boundary between the ultra-cataclastic fault core and the surrounding material has $\alpha \approx 10^{-1}$. This issue emerges also at the scale of fault systems and explains differences in inferred fractal geometry of the San Andreas fault in the studies of Okubo and Aki (1987) and Aviles *et al.* (1987).

Recent studies by Renard *et al.* (2006), Sagy *et al.* (2007), Sagy and Brodsky (2009), and Candela *et al.* (2009) have provided high-resolution data on fault surface roughness at scales of ~10 μm to ~100 m. The lower end of this range is covered by laboratory profilometers and the upper end by LiDAR scans. Analysis of this data, particularly by Candela *et al.* (2009), indicates that over the range of wavelengths spanned by a single instrument the surfaces are self-affine rather than self-similar. Self-affine surfaces, which have $\beta < 3$, appear smoother at larger scales. Values of β in the direction of slip are between 2.0 and 2.6 (corresponding to Hurst exponents between 0.5 and 0.8, rather than 1 for a self-similar profile). Similarly, high-resolution data has not yet been compiled at scales above ~100 m. Furthermore, not all studies find that a single power law spectral density function can simultaneously fit data from both the laboratory and outcrop scales. Because of this, we have chosen in this work to model faults as self-similar surfaces.

Consequences of Fault Roughness

Several authors have investigated how deviations from planarity influence fault mechanics. Saucier *et al.* (1992) studied stress perturbations induced by slip on a frictionless nonplanar fault; they suggested that fault curvature might help explain the unexpected orientation of the principal stresses around the San Andreas fault measured at the Cajon Pass borehole. Using a boundary perturbation approach, Chester and Chester (2000) demonstrated that stress perturbations due to slip on a frictional sinusoidal fault are most pronounced at the shortest wavelengths and increase with cumulative slip (at least when assuming elastic off-fault behavior). They furthermore made quantitative predictions of the location and extent of regions in which stresses are expected to activate inelastic deformation, according to a Mohr–Coulomb failure criterion. This boundary perturbation analysis is reviewed and extended to arbitrary profiles in the Appendix. More recently, Dieterich and Smith (2009) studied rough faults with the boundary element method. They found that roughness causes departures from the expected linear scaling of slip with fault length, if one assumes linear elastic response of the off-fault material. They then postulate that relaxation of the roughness-induced stress perturbations occurs via brittle failure processes (aftershocks and secondary faulting) in the surrounding material. They demonstrate how these relaxation processes restore the linear slip-length scaling and are roughly consistent with the decay of aftershock seismicity with distance from the fault.

Even minor amounts of roughness can induce large stress perturbations during slip. Unlike the rms roughness, which is determined by the longest wavelengths, the stress perturbations are dominated by the shortest wavelengths. As derived in the Appendix, the rms normal stress perturbation arising from roughness at wavenumbers between $k_{\min} = 0$ and $k_{\max} = 2\pi/\lambda_{\min}$ on a self-similar fault having slip Δu is

$$\Delta\sigma_{\mathrm{rms}}(0, 2\pi/\lambda_{\min}) = 2\pi^2\alpha\frac{G}{1-\nu}\frac{\Delta u}{\lambda_{\min}}. \tag{16}$$

Accompanying slip Δu on a nonplanar fault are fault-normal displacements $\sim\alpha\Delta u$. These are distributed over the wavelength of the roughness feature, λ, thereby inducing strains $\sim\alpha\Delta u/\lambda$. Multiplying these strains by the elastic stiffness, $G/(1-\nu)$, where G is the shear modulus and ν is Poisson's ratio, gives the normal stress perturbations shown in equation (16). The largest strains occur when the fault-normal displacements are accommodated over the shortest scales. Hence, the largest stress perturbations arise on faults that have large amounts of slip and short wavelength roughness. Taking $G = 30$ GPa and $\nu = 1/4$,

$$\Delta\sigma_{\mathrm{rms}}(0, 2\pi/\lambda_{\min}) \approx 160\ \mathrm{MPa}\left(\frac{\alpha}{10^{-3}}\right)\left(\frac{\Delta u}{1\,\mathrm{m}}\right)\left(\frac{10\,\mathrm{m}}{\lambda_{\min}}\right). \tag{17}$$

Such perturbations can easily become large enough to induce fault opening (so long as the material response remains ideally elastic) and/or inelastic off-fault deformation. We can estimate when fault opening is expected by comparing the rms normal stress perturbations to the effective normal stress on a flat fault, $-\sigma^0_{yy}$. Opening is expected if

$$\frac{\Delta u}{\lambda_{\min}} > \frac{-\sigma^0_{yy}(1-\nu)}{2\pi^2\alpha G}. \tag{18}$$

For a typical mid-seismogenic depth value of $-\sigma^0_{yy} =$ 100 MPa, opening is predicted to occur when $\Delta u/\lambda_{\min} \sim 0.1$ for $\alpha = 10^{-3}$ and when $\Delta u/\lambda_{\min} \sim 0.01$ for $\alpha = 10^{-2}$. In order to prevent opening (assuming ideally elastic off-fault response) when all roughness wavelengths down to the scale of slip are taken into account, then $\alpha < 10^{-4}$.

The previously described estimates clearly indicate the importance of fault roughness, but are almost certainly overpredictions due to the assumed elastic behavior of the off-fault material. Natural faults are surrounded by damage zones of high fracture density. These regions are the signature of inelastic deformation processes; it is reasonable to expect that during additional slip events, their response will involve further inelastic deformation. In this work we model the off-fault material as an elastic-plastic solid with a shear yield strength that depends on the mean effective stress, as understood by Mohr–Coulomb theory. Such material descriptions are well known to describe the behavior of rock (e.g., Jaeger *et al.*, 2007). In this work we neglect the effects of pore fluids.

An additional consequence of fault roughness is to introduce heterogeneity in slip. For quasi-static sliding at constant friction coefficient f, the slip perturbations are $fm(x)\Delta u$, where Δu is the average slip on the fault (see the Appendix). Hence, the slip perturbations, at least in this quasi-static analysis, are expected to be correlated with the local fault slope and to have the same statistical properties.

Model Description

Using 2D plane strain models, we study rupture propagation on nonplanar faults with strongly rate-weakening friction on the fault and inelastic deformation of the material surrounding the fault. The medium is assumed to be homogeneous and infinite in extent. The fault is the curve $y = h(x)$, which deviates only slightly from $y = 0$. Bandlimited self-similar profiles having amplitude-to-wavelength ratio α are generated using a Fourier synthesis method to obtain the desired power spectrum (e.g., Russ, 1994; Sahimi, 1998). We ensure accuracy of our numerical models by restricting the range of roughness wavelengths to those between $\lambda_{\min} = 20\Delta x$, where Δx is the grid spacing and the full extent of the spatial domain. (For some problems, we also verify the accuracy of the numerical solution by further decreasing Δx by a factor of 2 or 4 with all other lengths, including $\lambda_{\min}$, held fixed.) We consider only a single realization of the random surface, as shown in Figure 1, and reserve for later work investigations into variability of our results.

Some aspects of the numerical method, which is based on an unstaggered velocity-stress finite difference scheme, are presented in Part 1 and in Kozdon *et al.* (2011). The irregular geometry is handled using a coordinate transformation that maps a boundary-conforming mesh in the physical domain to a Cartesian mesh in the computational domain. The governing equations are transformed using the chain rule and numerically approximated with high-order finite differences in this new coordinate system. A similar procedure has been used for rupture dynamics by Kase and Day (2006). The mesh is generated by specifying points on the boundary curves and using transfinite interpolation (Boyd, 2001, p. 115) to provide the locations of the interior grid points. The partial derivatives of the mapping are computed numerically with the difference operators.

A complete description of the friction law and plasticity model is given in Part 1, but we summarize the relevant details here. The off-fault material is described by an elastic-viscoplastic Drucker–Prager rheology without cohesion. The coefficient of friction obeys a rate-and-state law that features the direct effect and evolution, over slip L, toward a strongly velocity-weakening steady state friction coefficient. Such laws give rise to self-healing slip pulses when the background shear stress, τ^b, is sufficiently low (specifically, around the critical value τ^{pulse}; (Zheng and Rice, 1998). For the parameters used in this work, $\tau^{\text{pulse}} = 0.2429\sigma^0$ for planar faults, where σ^0 is the initial normal stress acting on the fault (taken to be positive in compression). We restrict our attention in this work to ruptures in the slip pulse mode. In our model, shear strength is directly proportional to normal stress. Laboratory experiments (Linker and Dieterich, 1992; Prakash, 1998) suggest a delayed response of shear strength to normal stress perturbations, which might diminish the effects of stress perturbations from fault roughness. We do not expect our neglect of this effect to influence our results, as the evolution times inferred from experiments are far shorter than the transit time of a rupture across the minimum roughness wavelength in our model.

Parameters are identical to those in Part 1. The S-wave speed is c_s, and the shear modulus is G. The extent of the state-evolution region at the rupture front, over which the strength drop occurs, is characterized by a length scale R_0. The characteristic dynamic stress drop is $\Delta\tau$, and the peak strength is τ^p. We present both nondimensional and dimensional results; the latter use $c_s = 3.464$ km/s, $G = 32.04$ GPa, $\Delta\tau = 7.1195$ MPa, $\tau^p = 0.7\sigma^0$, and $R_0 = 300$ m. The viscoplastic relaxation time, η/G, is $0.1R_0/c_s$. The grid spacing is $\Delta x = R_0/16$, and the spatial domain is $-100R_0 \le x \le 200R_0$ and $-75R_0 \le y \le 75R_0$.

We assume a uniform initial stress field, which results in spatially heterogeneous initial shear and normal tractions on the nonplanar fault surface. An important parameter in determining the location of plastic deformation is the angle, Ψ, between the maximum compressive principal stress and the plane $y = 0$ (see Fig. 1a). We also assume that the material above and below the fault is initially moving in only the x direction at an extremely small constant rate (that motion is required with rate-and-state friction laws when $\tau^b \neq 0$). When resolved on the fault, the initial slip rate is heterogeneous, and the initial state variable is chosen to be consistent with these initial conditions (hence, it will be heterogeneous). The initial velocity field slightly violates the no-opening condition, which is enforced at the start of the simulation. This results in radiation of negligibly small amplitude waves (velocities about 10 orders of magnitude less than coseismic ones). This procedure is certainly not unique, and selection of realistic initial conditions should be a high priority for future studies.

Ruptures on Rough Faults

Having established the basic phenomenology of ruptures on flat faults with strongly rate-weakening friction and off-fault plasticity in Part 1, we now consider the influence of fault roughness. In no simulations do we observe any fault opening. That would require, if the fault were constrained against opening, tensile stress states, which are ruled out by our choice of a cohesionless yield surface. We note that opening, over large portions of the fault ($\sim 10R_0 = 3$ km or larger in some cases), was a common feature in earlier simulations we conducted assuming linear elastic off-fault response.

An important dimensionless parameter for ruptures on nonplanar faults is the ratio of a roughness wavelength to the

spatial extent of the strength-drop region at the rupture front, λ/R_0. When $\lambda/R_0 \gg 1$, then the rupture will be able to accelerate or decelerate over timescales much shorter than the time required for the rupture to traverse the roughness wavelength. In all of our simulations, $\lambda_{\min}/R_0 = 1.25$. In the opposite limit ($\lambda/R_0 \ll 1$), the rupture will probably only sense average properties of the fault because it is unlikely that rupture velocity will fluctuate over distances less than R_0. However, these short wavelengths of roughness may hinder propagation by providing energy loss through increased plastic deformation and high-frequency radiation. It is beyond the scope of this work to address this issue, which merits further study.

Increasing the amplitude-to-wavelength ratio of roughness, α, increases the critical background shear stress level at which self-sustaining propagation is just barely possible. Figure 2 shows slip profiles for $\Psi = 50°$ as a function of α. We increase the background stress, τ^b, the minimum amount to ensure propagation near the critical conditions (otherwise ruptures will arrest soon after nucleation). As α and τ^b are increased in this manner, the fluctuations in slip increase and the average rupture velocity decreases. Note, however, that the average slip remains roughly constant despite the increase in τ^b. We suspect that a similar amount of strain energy is being liberated in each case. The cases with larger α have higher initial strain energies due to the increase in τ^b. One might expect that because the coseismic strength of the faults is roughly identical, then ruptures with larger τ^b would liberate more strain energy, and slip would increase. This is evidently not true, and we speculate that for the rougher faults, the additional strain energy required to overcome the resistance to slip from geometric complexity is transferred during slip from the entire medium to stress concentrations around fault bends.

In Figures 3 and 4, we focus on two examples, both having $\alpha = 10^{-2}$ but different values of Ψ (20° and 50°). At lower values of Ψ, for which yielding on the extensional side is not so strongly favored, the stress perturbations due to roughness cause plastic flow on both sides of the fault. For higher values of Ψ, almost all of the plastic strain occurs on the extensional side of the fault, as it does for a flat fault, but stress perturbations due to nonplanarity modulate the amount of plastic strain. There are thus fluctuations in the rate of energy dissipation in the material surrounding the rupture front that possibly enhance variability in the rupture propagation speed.

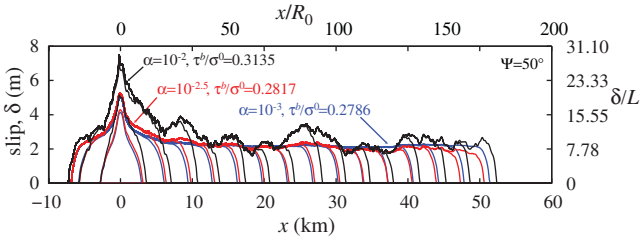

Figure 2. Profiles of slip (with time interval $16R_0/c_s = 1.3857$ s) for $\Psi = 50°$, illustrating the increase in slip heterogeneity as the amplitude-to-wavelength ratio of roughness, α, is increased. For all cases, the background stress, τ^b, is just slightly above that required for self-sustaining propagation. While this value of τ^b increases with α, the average amount of slip remains roughly constant. Results for a flat fault with $\tau^b = 0.2778\sigma^0$ (not shown) are quite similar to those with $\alpha = 10^{-3}$. The color version of this figure is available only in the electronic edition.

The location of intense plastic straining relative to specific nonplanar features depends on Ψ. There is some suggestion that regions of high plastic strain in the low Ψ case are regions of minimal plastic strain in the high Ψ case (e.g., around the bump at $x = 42$ km in Fig. 3). Similarly, in comparing the slip distributions for $\Psi = 20°$ and 50° in Figure 3, it is evident that regions of higher-than-average slip for $\Psi = 20°$ often have lower-than-average slip for $\Psi = 50°$ and vice-versa.

Figure 4 shows the local rupture velocity, $v_r(x)$, for these two cases. Rupture velocity is calculated as the inverse of the spatial derivative of rupture front arrival time, defined as the time at which slip first reaches the state-evolution distance. When yielding occurs on just one side of the fault (as for $\Psi = 50°$, for example), there is a clear relationship between rupture speed and the local fault slope. At reasonably high rupture speeds, the plane ahead of the rupture front that is most favorably oriented for frictional slip is inclined at an angle with respect to the current propagation direction (e.g., Poliakov *et al.*, 2002; Rice *et al.*, 2005); that angle depends on both rupture velocity and Ψ. Ruptures would thus branch onto a more favorably oriented fault, if one existed. For nonplanar faults with sufficiently large Ψ, this effect causes the rupture to accelerate when the fault bends into the extensional quadrant and to decelerate when the fault bends in the opposite direction. This explains the pronounced anticorrelation (correlation coefficient −0.83) of $v_r(x)$ and $m(x)$ for $\Psi = 50°$. For $\Psi = 20°$, there is a slight positive correlation (correlation coefficient 0.18). Similar relationships between rupture velocity and fault orientation have been noted by Kase and Day (2006), Oglesby *et al.* (2008), and others.

High-Frequency Ground Motion

The irregular rupture propagation observed in our rough fault models (e.g., Fig. 4) leads to the generation of high-frequency seismic waves. Our focus here is on strong ground motion in the near-source region, that is, the region within about one source dimension from the fault (which is the extent of our computational domain). Studies of far-field strong motion records by Hanks and McGuire (1981) suggest that acceleration time series from direct shear-wave arrivals are, to a reasonable level of approximation, bandlimited white noise. That is, the power spectral density of appropriately windowed far-field acceleration records is independent of frequency over a range of frequencies between the corner frequency, f_0, of the earthquake and the highest frequency,

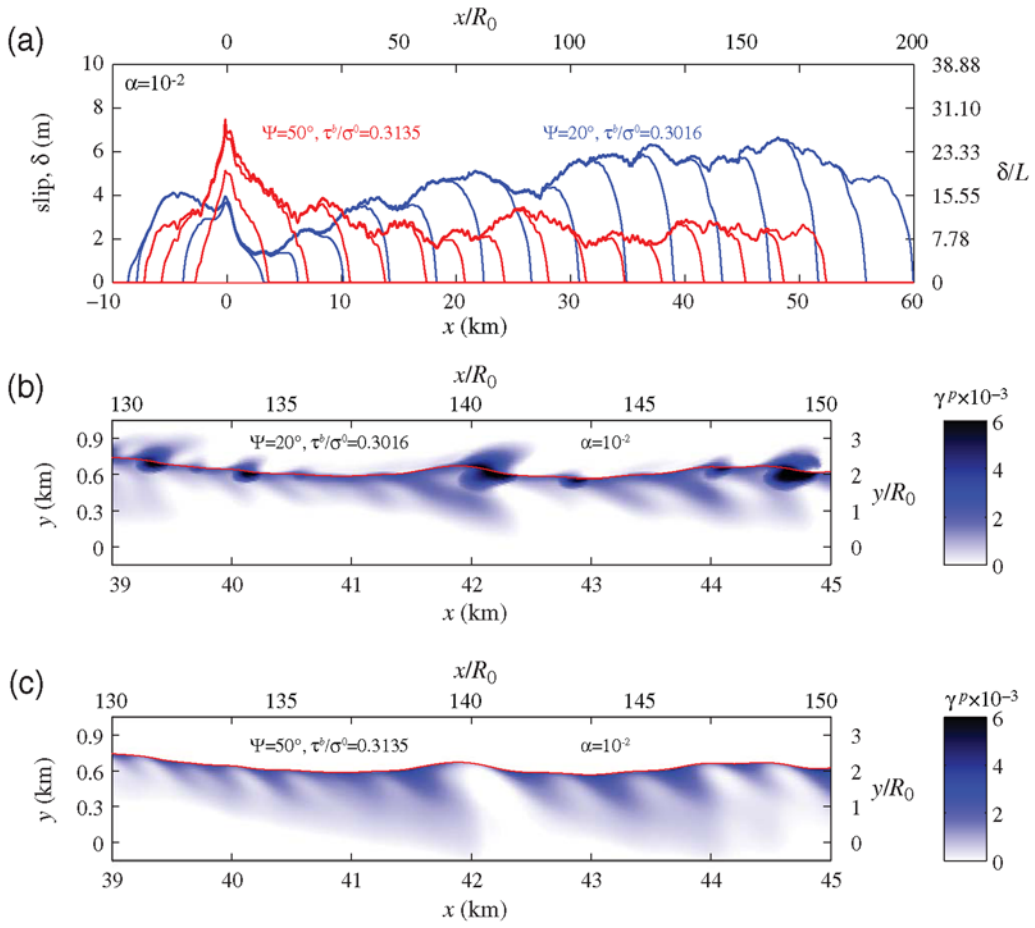

Figure 3. (a) Profiles of slip (with time interval $16R_0/c_s = 1.3857$ s) for $\Psi = 20°$ and 50°, both with $\alpha = 10^{-2}$. Zoomed-in views of equivalent plastic strain, γ^p, for (b) $\Psi = 20°$ and (c) $\Psi = 50°$. Plastic strain can be normalized by $\tau^p/2G = 1.38 \times 10^{-3}$. The color version of this figure is available only in the electronic edition.

$f_{\max}$, that remains undiminished by attenuation along the source-to-site path. Andrews (1981) has shown that the high-frequency spectral properties in the near-field region are the same as those in the far-field. Of course, acceleration records are not stationary stochastic signals (Iyengar and Iyengar, 1969); there is a finite duration of shaking that is important when predicting intensity measures from random vibration theory (Boore, 1983). Further scrutiny reveals a shift from shorter to longer periods over the duration of the record, and there have been efforts to generate synthetic seismograms with the same property (Der Kiureghian and Crempien, 1989). This is of critical importance for earthquake engineering, as the fundamental frequency of a building evolves with progressive accumulation of damage. In this section, we demonstrate how these observational characteristics emerge in our models. We focus on ground motion at a station located at $(x, y) = (87.5, 5.6)R_0 = (26.25, 1.68)$ km; see Figure 1a.

We begin with faults whose profiles contain only a single Fourier mode λ, that is, $h(x) = \alpha\lambda \sin(2\pi x/\lambda)$. In Figure 5 we use a space-time diagram to link ground motion to the fault profile. Even though the fault has a single characteristic wavelength, λ, the period of the ground motion oscillations changes with time. This feature is simply explained in terms of the Doppler shift due to the motion of the rupture first toward and then away from the station. To quantify this, assume that the rupture propagates at an average velocity $\bar{v}_r$, such that it repeatedly encounters the same fault topography at a time interval of $\lambda/\bar{v}_r$. Assuming that the ground motion oscillations are primarily caused by radiating shear waves, and making the approximation that λ is much smaller than the source-to-station distance, the expected period of the ground motion oscillations, T, is predicted to be

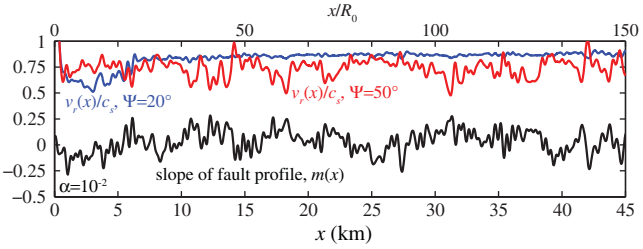

Figure 4. Relation between rupture velocity, $v_r(x)$, and slope of fault profile, $m(x)$, for $\Psi = 20°$ and 50° with $\alpha = 10^{-2}$. The color version of this figure is available only in the electronic edition.

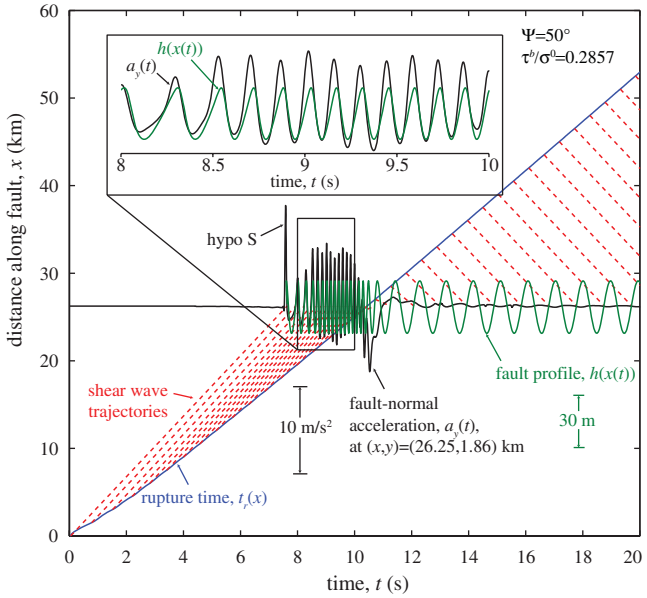

Figure 5. Space-time diagram of rupture on a sinusoidal fault $h(x) = \alpha\lambda \sin(2\pi x/\lambda)$ having wavelength $\lambda = 1.5$ km and $\alpha = 10^{-2}$. Fault-normal acceleration, $a_y(t)$, is shown at the station in Figure 1a. The large acceleration spike at $t \approx 7.5$ s is the hypocentral shear-wave arrival, which is unreasonably large because of the abrupt artificial nucleation process. Also shown is the rupture front arrival time, $t_r(x)$; the rupture speed has average value $\bar{v}_r$ and fluctuations with period $\lambda/\bar{v}_r$. High-frequency waves are emitted at this period; their trajectories through space-time to the station are shown with dashed lines. A shear wave emitted from the fault at $(x, y) = [x, h(x)]$ arrives at the station at (x_s, y_s) at time $t = t_r(x) + \sqrt{(x_s - x)^2 + [y_s - h(x)]^2}/c_s$; this equation can be inverted for $x = x(t)$, the fault location causing the ground motion signal recorded at time t. Using this relation, the fault profile $y = h(x)$ is plotted as a function of time ($h[x(t)]$), making it is possible to directly relate the fault profile to the acceleration record (see inset for more detail). The Doppler effect explains the increase in ground motion period when the rupture passes the station at $t \approx 10.5$ s. The color version of this figure is available only in the electronic edition.

$$T \approx \frac{\lambda}{\bar{v}_r}\left(1 - \frac{\bar{v}_r}{c_s}\cos\theta\right), \tag{19}$$

where θ is the angle between a line passing through the center of the fault (i.e., $y = 0$), and a line connecting the station to the section of the fault from which waves recorded at the time of interest were emitted. Hence, θ increases from roughly 0 to $\pi/2$ to π as the rupture approaches, passes, and then recedes from the station. The period thus increases monotonically from $(\lambda/\bar{v}_r)(1 - \bar{v}_r/c_s)$ to $(\lambda/\bar{v}_r)(1 + \bar{v}_r/c_s)$ as the rupture passes. A close examination of Figure 5 supports this quantitative interpretation. While there are other explanations for the changing frequency content of seismograms at farther distances from the fault (e.g., the arrival of longer-period surface waves after direct body-wave arrivals), the Doppler effect is a likely explanation in the near-source region.

When roughness makes only small perturbations to the rupture process (as occurs when conditions are not too close to the critical ones), we find that while the period of ground motion oscillations is of order λ/c_s, the amplitude depends primarily on the amplitude-to-wavelength ratio α (rather than the amplitude of the profile, $\alpha\lambda$). However, when conditions are close to critical ones, the response becomes highly nonlinear and such simple relations do not exist.

Next, we turn to ruptures on self-similar faults. Figures 6 and 7 show synthetic seismograms and Fourier acceleration spectra at the same station for several values of α and $\Psi = 50°$ (same cases as shown in Fig. 2). Also shown are two near-field strong motion records from strike-slip events: the Lucerne Valley (LUC) record from the 1992 M_w 7.3 Landers, California, earthquake and the TTRH02 borehole record from the 2000 M_w 6.6 Tottori, Japan, earthquake. LUC was located about 2 km from the fault (Wald and Heaton, 1994), and the LUC record is widely considered to be representative of near-source ground motions expected from large subshear ruptures. The record has been rotated into fault-normal and fault-parallel components using the average strike of the fault system (336°). The record has been corrected by Chen (1995), and the instrument correction filter passes frequencies up to about 25 Hz. TTRH02 is thought to be nearly on top of the fault hosting the Tottori rupture (Semmane *et al.*, 2005), but lack of surface rupture near

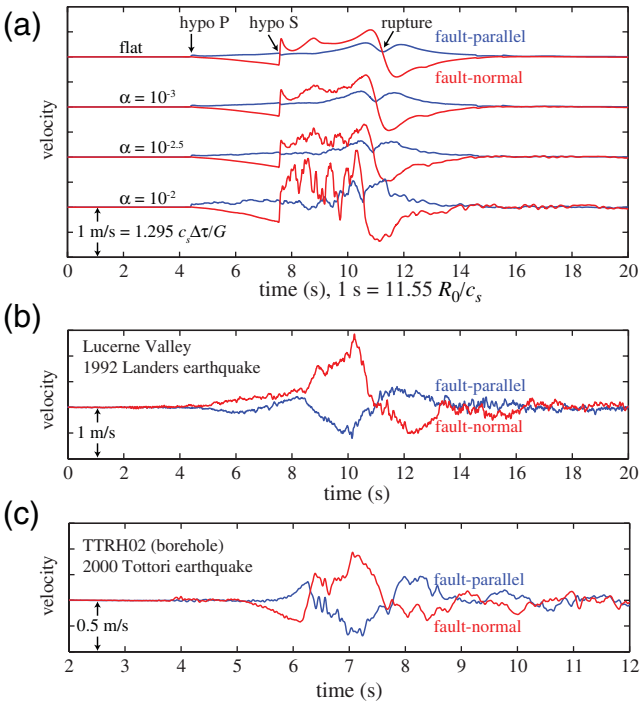

Figure 6. (a) Synthetic velocity seismograms for several values of the amplitude-to-wavelength ratio α, with flat fault case ($\alpha = 0$) for reference. Hypocentral *P*- and *S*-wave arrivals are marked; the two-sided fault-normal pulse occurs when the rupture passes the station. (b) Lucerne Valley record from the 1992 M_w 7.3 Landers earthquake. (c) TTRH02 borehole record from the 2000 M_w 6.6 Tottori earthquake (note different timescale due to smaller magnitude). The color version of this figure is available only in the electronic edition.

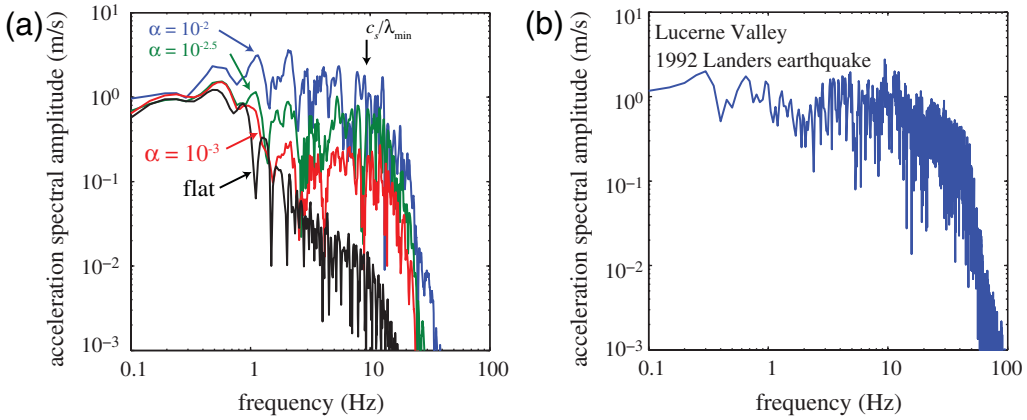

Figure 7. (a) Fourier amplitude spectra (FAS) of fault-normal acceleration corresponding to seismograms in Figure 6a windowed between 8 and 20 s to avoid the overly sharp hypocentral *S*-wave arrival due to the artificial nucleation. The absence of roughness wavelengths below λ_{min} prevents the excitation of waves at frequencies greater than $\sim c_s/\lambda_{min}$. (b) FAS of Lucerne Valley record (fault-normal component) shown in Figure 6b. The color version of this figure is available only in the electronic edition.

the station prevents quantification of the distance between the fault and the station. We have rotated this record to the average local strike of the fault system, 146° (Fukuyama *et al.*, 2003).

The comparison of our synthetic seismograms and the strong motion records is only meant to be qualitative, given the 2D nature of our simulations. However, the main features are remarkably similar. Beginning with the hypocentral *P*-wave arrival, the fault-normal component begins a gradual decrease until the hypocentral *S*-wave arrives; this motion comes from the near-field and intermediate-field *P*-wave terms (Aki and Richards, 2002). This is seen in our synthetics and the TTRH02 record but has the wrong sign in the LUC record. This might be due to the significant change in strike of the fault segments hosting the Landers rupture or the instrumental correction that was applied to recover long-period static offsets (Chen, 1995). Sustained strong shaking with positive fault-normal velocity commences with the hypocentral *S*-wave arrival and continues as shear waves radiated ahead of the rupture arrive at the station. These motions are seen between 7.5 and 10.5 s in the synthetics, 8.5 and 10 s in the LUC record, and 6.5 and 7.2 s in the TTRH02 record. Amplitudes are large due to forward directivity. The high-frequency oscillations arise from short bursts of radiation that occur when the rupture accelerates or decelerates, as seen in Figure 8. Shaking subsides as the rupture passes, which provides the negative fault-normal motion that completes the well-known two-sided velocity pulse.

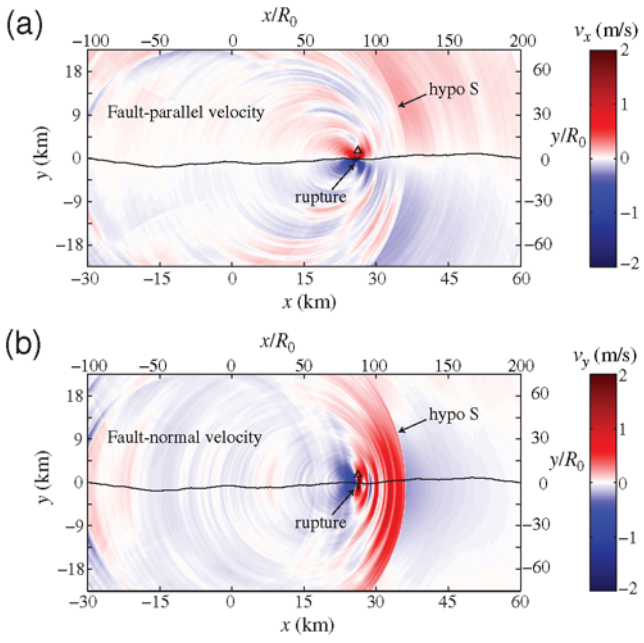

Figure 8. Snapshots (at time $t = 120R_0/c_s = 10.3926$ s) of the velocity field for $\alpha = 10^{-2}$ as the rupture passes the station (triangle) at which seismograms in Figure 6 are calculated: (a) fault-parallel (v_x); (b) fault-normal (v_y). The hypocentral shear wave is marked "hypo S." Note that 1 m/s $= 1.295 c_s \Delta\tau/G$. The color version of this figure is available only in the electronic edition.

Discussion

We have investigated the role of fault roughness in the earthquake rupture process, using numerical simulations that include both strongly rate-weakening fault friction and off-fault plasticity. Accounting for inelastic deformation near the fault is essential to prevent large-scale fault opening. Roughness with amplitude-to-wavelength ratios between 10^{-3} and 10^{-2} leads to an irregular rupture process, even if the initial stress field is spatially uniform. This irregularity manifests itself in heterogeneous slip distributions and fluctuations in rupture velocity; both contribute to high-frequency ground motion.

As expected, production of high-frequency radiation increases with increasing levels of roughness (specifically, the amplitude-to-wavelength ratio α). In addition, high-frequency waves are most efficiently generated when the background stress is just barely larger than the critical level

required for self-sustaining propagation; under these conditions, the response becomes quite nonlinear, and slight perturbations in the fault profile can cause substantial changes in the propagation process. Thus, two ruptures on the same fault may produce different amounts of high-frequency radiation if there are differences in the background stress level.

Our simulations leave open several issues. The first is dimensionality. There are differences between 2D and 3D wave propagation in terms of both geometric spreading and the extended duration of influence of disturbances in two dimensions (i.e., the "tail" behind wavefronts in the 2D Green's function). Additionally, we expect that accounting for surface roughness in the unmodeled dimension (z direction) will increase irregularity of the ground motion; our plane strain simulations effectively force coherence of the rupture process in the z direction.

Second, our models only account for fault roughness over a limited range of wavelengths. Our minimum modeled wavelengths are ~100 m, but with additional computational resources it will be possible to include wavelengths down to the scale of slip (at which point the assumption of grid points collocated on either side of the fault breaks down, and the numerical method would need to be altered). Additionally, given the larger amplitude of stress perturbations and the additional resistance to slip introduced at short wavelengths, we expect there may be substantial changes in the predicted minimum background stress level at which faults are capable of hosting ruptures.

Third, we have assumed, for simplicity, a spatially uniform initial stress field. Slip introduces heterogeneities in the stress field; these become the initial conditions for subsequent events, and most certainly will influence the rupture process. We have not attempted to simulate multiple events and interseismic deformation on a single fault, but this must be done in order to have self-consistent initial conditions.

Finally, we have investigated only one possible source of high-frequency ground motion, and it is undoubtedly the case that both scattering along the path and local site conditions play a role in nature. There is a clear need for more extensive numerical modeling to resolve all of these issues.

Data and Resources

The Lucerne Valley record was from the COSMOS strong motion data center (db.cosmos-eq.org, last accessed February 2010); the TTRH02 record was from the Japanese KiK-net database (www.kik.bosai.go.jp, last accessed April 2009). The numerical simulations were conducted at the Stanford Center for Computational Earth and Environmental Science with computational support by Dennis Michael and Robert Clapp; at the Texas Advanced Computer Center (TACC) through a TeraGrid allocation; and on Harvard's BlueGene/L with support by Jayanta Sircar, Seppo Sahrakorpi, Suvendra Dutta, and the SEAS Cyberinfrastructure Lab.

Acknowledgments

This work was initiated when E.M.D., D.B., and L.C. were at Harvard University. Work there was supported by the Southern California Earthquake Center (SCEC) as funded by Cooperative Agreements NSF EAR-0529922 and USGS 07HQAG0008, the Harvard Faculty Aide program for undergraduate research (under the supervision of James R. Rice), matching funds from Harvard's Department of Earth and Planetary Sciences, and an award from the Highbridge Undergraduate Research Fund through Harvard's Department of Mathematics to D.B. Later work at Stanford by E.M.D. and J.E.K. was supported by NSF award EAR-0910574 and by SCEC (SCEC contribution number 1413). Discussions with James R. Rice, Elizabeth L. Templeton, Robert C. Viesca, and Emily E. Brodsky throughout this project were invaluable. The insightful comments of Steven M. Day, David D. Oglesby, and an anonymous reviewer improved the manuscript.

References

Aki, K., and P. Richards (2002). *Quantitative Seismology*, University Science Books, Sausalito, California.

Andrews, D. J. (1980). A stochastic fault model, 1. Static case, *J. Geophys. Res.* **85,** 3867–3877.

Andrews, D. J. (1981). A stochastic fault model, 2. Time-dependent case, *J. Geophys. Res.* **86,** no. B11, 10,821–10,834.

Andrews, D. J. (2005). Rupture dynamics with energy loss outside the slip zone, *J. Geophys. Res.* **110,** B01307, doi 10.1029/2004JB003191.

Aviles, C. A., C. H. Scholz, and J. Boatwright (1987). Fractal analysis applied to characteristics segments of the San Andreas fault, *J. Geophys. Res.* **92,** no. B1, 331–344.

Beeler, N. M., T. E. Tullis, and D. L. Goldsby (2008). Constitutive relationships and physical basis of fault strength due to flash heating, *J. Geophys. Res.* **113,** B01401, doi 10.1029/2007JB004988.

Ben-Zion, Y., and Z. Shi (2005). Dynamic rupture on a material interface with spontaneous generation of plastic strain in the bulk, *Earth Planet. Sci. Lett.* **236,** 486–496, doi 10.1016/j.epsl.2005.03.025.

Boore, D. M. (1983). Stochastic simulation of high-frequency ground motions based on seismological models of the radiated spectra, *Bull. Seismol. Soc. Am.* **73,** no. 6, 1865–1894.

Boore, D. M. (2003). Simulation of ground motion using the stochastic method, *Pure Appl. Geophys.* **160,** 635–676.

Boore, D. M., and W. B. Joyner (1978). The influence of rupture incoherence on seismic directivity, *Bull. Seismol. Soc. Am.* **68,** no. 2, 283–300.

Boyd, J. P. (2001). *Chebyshev and Fourier Spectral Methods*, Dover, New York.

Brown, S. R., and C. H. Scholz (1985). Broad bandwidth study of the topography of natural rock surfaces, *J. Geophys. Res.* **90,** no. B14, 12,575–12,582.

Candela, T., F. Renard, M. Bouchon, A. Brouste, D. Marsan, J. Schmittbuhl, and C. Voisin (2009). Characterization of fault roughness at various scales: Implications of three-dimensional high resolution topography measurements, *Pure Appl. Geophys.* **166,** no. 10, 1817–1851, doi 10.1007/s00024-009-0521-2.

Chen, X. (1995). Near-field ground motion from the Landers earthquake, *Tech. Rep. Caltech EERL:1995.EERL-95-02*, California Institute of Technology.

Chester, F. M., and J. S. Chester (2000). Stress and deformation along wavy frictional faults, *J. Geophys. Res.* **105,** no. B10, 23,421–23,430.

Chester, F. M., J. S. Chester, D. L. Kirschner, S. E. Schulz, and J. P. Evans (2004). Structure of large-displacement, strike-slip fault zones in the brittle continental crust, in *Rheology and Deformation in the Lithosphere at Continental Margins*, edited by G. D. Karner, B. Taylor, N. W. Driscoll, and D. L. Kohlstedt, pp. 223–260, Columbia Univ. Press, New York.

Der Kiureghian, A., and J. Crempien (1989). An evolutionary model for earthquake ground motion, *Struct. Safety* **6,** 235–246.

Di Toro, G., D. L. Goldsby, and T. E. Tullis (2004). Friction falls toward zero in quartz rock as slip velocity approaches seismic rates, *Nature* **427,** 436–439, doi 10.1038/nature02249.

Dieterich, J. H., and D. E. Smith (2009). Nonplanar faults: Mechanics of slip and off-fault damage, *Pure Appl. Geophys.* **166,** no. 10, 1799–1815, doi 10.1007/s00024-009-0517-y.

Duan, B., and S. M. Day (2008). Inelastic strain distribution and seismic radiation from rupture of a fault kink, *J. Geophys. Res.* **113,** B12311, doi 10.1029/2008JB005847.

Dunham, E. M., D. Belanger, L. Cong, and J. E. Kozdon (2011). Earthquake ruptures with strongly rate-weakening friction and off-fault plasticity, Part 1: Planar faults, *Bull. Seismol. Soc. Am.*, **101,** 2296–2307.

Fukuyama, E., W. L. Ellsworth, F. Waldhauser, and A. Kubo (2003). Detailed fault structure of the 2000 Western Tottori, Japan, earthquake sequence, *Bull. Seismol. Soc. Am.* **93,** no. 4, 1468–1478, doi 10.1785/0120020123.

Geubelle, P. H., and J. R. Rice (1995). A spectral method for three-dimensional elastodynamic fracture problems, *J. Mech. Phys. Solids* **43,** 1791–1824.

Guatteri, M., P. M. Mai, G. C. Beroza, and J. Boatwright (2003). Strong ground motion prediction from stochastic-dynamic source models, *Bull. Seismol. Soc. Am.* **93,** no. 1, 301–313.

Hanks, T. C. (1979). b values and $\omega^{-\gamma}$ seismic source models: Implications for tectonic stress variations along active crustal fault zones and the estimation of high-frequency strong ground motion, *J. Geophys. Res.* **84,** no. B5, 2235–2242, doi 10.1029/JB084iB05p02235

Hanks, T. C., and R. K. McGuire (1981). The character of high-frequency strong ground motion, *Bull. Seismol. Soc. Am.* **71,** no. 6, 2071–2095.

Hartzell, S., S. Harmsen, A. Frankel, and S. Larsen (1999). Calculation of broadband time histories of ground motion: Comparison of methods and validation using strong-ground motion from the 1994 Northridge earthquake, *Bull. Seismol. Soc. Am.* **89,** no. 6, 1484–1504.

Haskell, N. A. (1964). Total energy and energy spectral density of elastic wave radiation from propagating faults, *Bull. Seismol. Soc. Am.* **54,** no. 6, 1811–1841.

Herrero, A., and P. Bernard (1994). A kinematic self-similar rupture process for earthquakes, *Bull. Seismol. Soc. Am.* **84,** no. 4, 1216–1228.

Hirose, T., and T. Shimamoto (2005). Growth of a molten zone as a mechanism of slip weakening of simulated faults in gabbro during frictional melting, *J. Geophys. Res.* **110,** B05202, doi 10.1029/2004JB003207.

Housner, G. W. (1947). Characteristics of strong-motion earthquakes, *Bull. Seismol. Soc. Am.* **37,** no. 1, 19–31.

Housner, G. W. (1955). Properties of strong ground motion earthquakes, *Bull. Seismol. Soc. Am.* **45,** no. 3, 197–218.

Iyengar, R. N., and K. T. S. R. Iyengar (1969). A nonstationary random process model for earthquake accelerograms, *Bull. Seismol. Soc. Am.* **59,** no. 3, 1163–1188.

Jaeger, J., N. Cook, and R. Zimmerman (2007). *Fundamentals of Rock Mechanics*, fourth ed., Blackwell Publishing Ltd, Malden, Massachusetts.

Kase, Y., and S. M. Day (2006). Spontaneous rupture processes on a bending fault, *Geophys. Res. Lett.* **33,** L10302, doi 10.1029/2006GL025870.

Kozdon, J. E., E. M. Dunham, and J. Nordström (2011). Interaction of waves with frictional interfaces using summation-by-parts difference operators: Weak enforcement of nonlinear boundary conditions, *J. Sci. Comp.*, doi 10.1007/s10915-011-9485-3.

Lee, J.-J., and R. L. Bruhn (1996). Structural anisotropy of normal fault surfaces, *J. Struct. Geol.* **18,** no. 8, 1043–1059.

Linker, M. F., and J. H. Dieterich (1992). Effects of variable normal stress on rock friction: Observations and constitutive equations, *J. Geophys. Res.* **97,** 4923–4940.

Ma, S., and G. C. Beroza (2008). Rupture dynamics on a bimaterial interface for dipping faults, *Bull. Seismol. Soc. Am.* **98,** no. 4, 1642–1658, doi 10.1785/0120070201.

Madariaga, R. (1977). High-frequency radiation from crack (stress drop) models of earthquake faulting, *Geophys. J. Roy. Astr. Soc.* **51,** 625–651.

Mai, P. M., and G. C. Beroza (2003). A hybrid method for calculating near-source, broadband seismograms: Application to strong motion prediction, *Pure Appl. Geophys.* **137,** 183–199, doi 10.1016/S0031-9201(03)00014-1.

McGuire, R. K., and T. C. Hanks (1980). RMS accelerations and spectral amplitudes of strong ground motion during the San Fernando, California earthquake, *Bull. Seismol. Soc. Am.* **70,** no. 5, 907–1919.

Newland, D. E. (1993). *An Introduction to Random Vibrations, Spectral & Wavelet Analysis*, Longman Scientific & Technical, Essex, England.

Oglesby, D. D., and S. M. Day (2002). Stochastic fault stress: Implications for fault dynamics and ground motion, *Bull. Seismol. Soc. Am.* **92,** 3006–3021.

Oglesby, D. D., P. M. Mai, K. Atakan, and S. Pucci (2008). Dynamic models of earthquakes on the North Anatolian fault zone under the Sea of Marmara: Effect of hypocenter location, *Geophys. Res. Lett.* **35,** L18302, doi 10.1029/2008GL035037.

Okubo, P. G., and K. Aki (1987). Fractal geometry in the San Andreas fault system, *J. Geophys. Res.* **92,** no. B1, 345–355, doi 10.1029/JB092iB01p00345.

Papageorgiou, A. S., and K. Aki (1983). A specific barrier model for the quantitative description of inhomogeneous faulting and the prediction of strong ground motion. i. description of the model, *Bull. Seismol. Soc. Am.* **73,** no. 3, 693–722.

Pitarka, A., P. Somerville, Y. Fukushima, T. Uetake, and K. Irikura (2000). Simulation of near-fault strong-ground motion using hybrid Green's functions, *Bull. Seismol. Soc. Am.* **3,** 566–586.

Poliakov, A. N. B., R. Dmowska, and J. R. Rice (2002). Dynamic shear rupture interactions with fault bends and off-axis secondary faulting, *J. Geophys. Res.* **107,** doi 10.1029/2001JB000572.

Power, W. L., and T. E. Tullis (1988). Roughness and wear during brittle faulting, *J. Geophys. Res.* **93,** no. B11, 15,268–15,278.

Power, W. L., and T. E. Tullis (1991). Euclidean and fractal models for the description of rock surface roughness, *J. Geophys. Res.* **96,** no. B1, 415–424.

Power, W. L., and T. E. Tullis (1995). Review of the fractal character of natural fault surfaces with implications for friction and the evolution of fault zones, in *Fractals in the Earth Sciences*, edited by C. C. Barton and P. R. L. Pointe, chap. 5, pp. 89–105, Plenum Press.

Prakash, V. (1998). Frictional response of sliding interfaces subjected to time varying normal pressures, *J. Tribol.* **120,** 97–102.

Prakash, V., and F. Yuan (2004). Results of a pilot study to investigate the feasibility of using new experimental techniques to measure sliding resistance at seismic slip rates, *SCEC Ann. Prog. Rep.*, Southern California Earthquake Center.

Renard, F., C. Voisin, D. Marsan, and J. Schmittbuhl (2006). High resolution 3D laser scanner measurements of a strike-slip fault quantify its morphological anisotropy at all scales, *Geophys. Res. Lett.* **33,** L04305, doi 10.1029/2005GL025038.

Resor, P. G., and V. E. Meer (2009). Slip heterogeneity on a corrugated fault, *Earth Planet. Sci. Lett.* **288,** 483–491, doi 10.1016/j.epsl.2009.10.010.

Rice, J. R., C. G. Sammis, and R. Parsons (2005). Off-fault secondary failure induced by a dynamic slip-pulse, *Bull. Seismol. Soc. Am.* **95,** no. 1, 109–134.

Ripperger, J., J.-P. Ampuero, P. M. Mai, and D. Giardini (2007). Earthquake source characteristics from dynamic rupture with constrained stochastic fault stress, *J. Geophys. Res.* **112,** B04311, doi 10.1029/2006JB004515.

Russ, J. C. (1994). *Fractal Surfaces*, Plenum Press, New York.

Sagy, A., and E. E. Brodsky (2009). Geometric and rheological asperities in an exposed fault zone, *J. Geophys. Res.* **114,** no. B2, B02301, doi 10.1029/2008JB005701.

Sagy, A., E. E. Brodsky, and G. J. Axen (2007). Evolution of fault-surface roughness with slip, *Geol.* **35,** no. 3, 283–286, doi 10.1130/G23235A.1.

Sahimi, M. (1998). Non-linear and non-local transport processes in heterogeneous media: from long-range correlated percolation to fracture and materials breakdown, *Phys. Rep.* **306,** 213–395.

Saikia, C. K., and P. G. Somerville (1997). Simulated hard-rock motions in Saint Louis, Missouri, from large New Madrid earthquakes ($M_w \geq 6.5$), *Bull. Seismol. Soc. Am.* **87,** 123–139.

Saucier, F., E. Humphreys, and R. Weldon (1992). Stress near geometrically complex strike-slip faults: Application to the San Andreas fault at Cajon Pass, Southern California, *J. Geophys. Res.* **97,** no. B4, 5081–5094, doi 10.1029/91JB02644.

Semmane, F., F. Cotton, and M. Campillo (2005). The 2000 Tottori earthquake: A shallow earthquake with no surface rupture and slip properties controlled by depth, *J. Geophys. Res.* **110,** B03306, doi 10.1029/2004JB003194.

Spudich, P., and L. N. Frazer (1984). Use of ray theory to calculate high-frequency radiation from earthquake sources having spatially variable rupture velocity and stress drop, *Bull. Seismol. Soc. Am.* **74,** 2061–2081.

Templeton, E. L., and J. R. Rice (2008). Off-fault plasticity and earthquake rupture dynamics: 1. Dry materials or neglect of fluid pressure changes, *J. Geophys. Res.* **113,** B09306, doi 10.1029/2007JB005529.

Tsutsumi, A., and T. Shimamoto (1997). High velocity frictional properties of gabbro, *Geophys. Res. Lett.* **24,** 699–702.

Tullis, T. E., and D. L. Goldsby (2003a). Flash melting of crustal rocks at almost seismic slip rates, *Eos Trans. AGU* **84,** no. 46, Fall Meet. Suppl., Abstract S51B-05.

Tullis, T. E., and D. L. Goldsby (2003b). Laboratory experiments on fault shear resistance relevant to coseismic earthquake slip, *SCEC Ann. Prog. Rep.*, Southern California Earthquake Center.

Viesca, R. C., E. L. Templeton, and J. R. Rice (2008). Off-fault plasticity and earthquake rupture dynamics: 2. Effects of fluid saturation, *J. Geophys. Res.* **113,** B09307, doi 10.1029/2007JB005530.

Wald, D. J., and T. H. Heaton (1994). Spatial and temporal distribution of slip for the 1992 Landers, California, earthquake, *Bull. Seismol. Soc. Am.* **84,** no. 3, 668–691.

Zheng, G., and J. R. Rice (1998). Conditions under which velocity-weakening friction allows a self-healing versus a cracklike mode of rupture, *Bull. Seismol. Soc. Am.* **88,** 1466–1483.

Zeng, Y., J. G. Anderson, and G. Yu (1994). A composite source model for computing realistic synthetic strong ground motions, *Geophys. Res. Lett.* **2,** no. 8, 725–728.

Appendix

First-Order Effects of Fault Nonplanarity

In this appendix we derive the first-order effects of roughness on frictional slip for static elasticity; similar analyses were conducted by Saucier *et al.* (1992) and Chester and Chester (2000). The problem is cast as a boundary perturbation problem. Two approximations are employed in this procedure, both of which involve an expansion in terms of a small dimensionless parameter ϵ that characterizes the amplitude of the height fluctuations. We express the slope as $m(x) = \epsilon\tilde{m}(x)$, the profile as $h(x) = \epsilon\tilde{h}(x)$, and assume that $\epsilon \ll 1$. Boundary conditions are naturally expressed in terms of fields defined in a local orthogonal coordinate system based on the unit normal and tangent to the irregular boundary. In transforming between the xy-coordinate system and the local tangential-normal coordinate system, we make use of the small-angle approximation. For example, the slip $\delta(x)$ at point $[x, y = h(x)]$, given by

$$\begin{aligned}\delta(x) = {} & \{u_x[x, h(x)^+] - u_x[x, h(x)^-]\}\cos\theta(x) \\ & + \{u_y[x, h(x)^+] - u_y[x, h(x)^-]\}\sin\theta(x), \end{aligned} \tag{A1}$$

for $\tan\theta(x) = m(x)$, is approximated as

$$\begin{aligned}\delta(x) &= u_x[x, h(x)^+] - u_x[x, h(x)^-] \\ &\quad + \epsilon\tilde{m}(x)\{u_y[x, h(x)^+] - u_y[x, h(x)^-]\} + O(\epsilon^2) \\ &= u_x[x, h(x)^+] - u_x[x, h(x)^-] \\ &\quad + m(x)\{u_y[x, h(x)^+] - u_y[x, h(x)^-]\} + O(\epsilon^2). \end{aligned} \tag{A2}$$

Rather than applying boundary conditions on $y = h(x)$, we can apply them on $y = 0$ with the aid of another approximation. A field $g(x, y)$ that is to be evaluated on the fault surface is approximated by Taylor series expansion as

$$\begin{aligned} g[x, h(x)] &= g(x, 0) + \epsilon\tilde{h}(x)\left.\frac{\partial g}{\partial y}\right|_{y=0} + O(\epsilon^2) \\ &= g(x, 0) + h(x)\left.\frac{\partial g}{\partial y}\right|_{y=0} + O(\epsilon^2). \end{aligned} \tag{A3}$$

Following this procedure and neglecting terms of $O(\epsilon^2)$, the slip $\delta(x)$, opening $\omega(x)$, shear stress $\tau(x)$, and normal stress $\sigma(x)$ on the fault are

$$\begin{aligned}\delta(x) = {} & u_x(x, 0^+) - u_x(x, 0^-) + m(x)[u_y(x, 0^+) \\ & - u_y(x, 0^-)] + h(x)\left(\left.\frac{\partial u_x}{\partial y}\right|_{y=0^+} - \left.\frac{\partial u_x}{\partial y}\right|_{y=0^-}\right), \end{aligned} \tag{A4}$$

$$\begin{aligned}\omega(x) = {} & u_y(x, 0^+) - u_y(x, 0^-) - m(x)[u_x(x, 0^+) \\ & - u_x(x, 0^-)] + h(x)\left(\left.\frac{\partial u_y}{\partial y}\right|_{y=0^+} - \left.\frac{\partial u_y}{\partial y}\right|_{y=0^-}\right), \end{aligned} \tag{A5}$$

$$\begin{aligned}\tau^{\pm}(x) = {} & \sigma_{xy}(x, 0^{\pm}) - m(x)[\sigma_{xx}(x, 0^{\pm}) - \sigma_{yy}(x, 0^{\pm})] \\ & + h(x)\left.\frac{\partial\sigma_{xy}}{\partial y}\right|_{y=0^{\pm}}, \end{aligned} \tag{A6}$$

$$\begin{aligned}\sigma^{\pm}(x) = {} & -\sigma_{yy}(x, 0^{\pm}) + 2m(x)\sigma_{xy}(x, 0^{\pm}) \\ & - h(x)\left.\frac{\partial\sigma_{yy}}{\partial y}\right|_{y=0^{\pm}}. \end{aligned} \tag{A7}$$

The $\pm$ symbol indicates fields that are defined on the top or bottom of the fault, that is, $y = h(x)^{\pm}$ or $y = 0^{\pm}$ after approximation. We will later enforce continuity of the traction components of stress, so we can write $\tau(x)$ in place of $\tau^{\pm}(x)$ without any confusion; the same applies to $\sigma(x) = \sigma^{\pm}(x)$.

The next step is to expand the solution in powers of ϵ:

$$u_i(x, y) = u_i^{(0)}(x, y) + \epsilon u_i^{(1)}(x, y) + O(\epsilon^2), \tag{A8}$$

$$\sigma_{ij}(x,y) = \sigma_{ij}^{(0)}(x,y) + \epsilon\sigma_{ij}^{(1)}(x,y) + O(\epsilon^2), \tag{A9}$$

and for notational convenience we write the first-order terms as

$$\hat{u}_i(x,y) = \epsilon u_i^{(1)}(x,y) \quad \text{and} \quad \hat{\sigma}_{ij}(x,y) = \epsilon\sigma_{ij}^{(1)}(x,y). \tag{A10}$$

Now substitute the expanded solution into the approximated expressions for fields on the fault and drop $O(\epsilon^2)$ terms:

$$\begin{aligned}\delta(x) = {} & u_x^{(0)}(x,0^+) - u_x^{(0)}(x,0^-) + \hat{u}_x(x,0^+) - \hat{u}_x(x,0^-) \\ & + m(x)[u_y^{(0)}(x,0^+) - u_y^{(0)}(x,0^-)] \\ & + h(x)\left(\frac{\partial u_x^{(0)}}{\partial y}\bigg|_{y=0^+} - \frac{\partial u_x^{(0)}}{\partial y}\bigg|_{y=0^-}\right),\end{aligned} \tag{A11}$$

$$\begin{aligned}\omega(x) = {} & u_y^{(0)}(x,0^+) - u_y^{(0)}(x,0^-) + \hat{u}_y(x,0^+) - \hat{u}_y(x,0^-) \\ & - m(x)[u_x^{(0)}(x,0^+) - u_x^{(0)}(x,0^-)] \\ & + h(x)\left(\frac{\partial u_y^{(0)}}{\partial y}\bigg|_{y=0^+} - \frac{\partial u_y^{(0)}}{\partial y}\bigg|_{y=0^-}\right),\end{aligned} \tag{A12}$$

$$\begin{aligned}\tau^{\pm}(x) = {} & \sigma_{xy}^{(0)}(x,0^{\pm}) + \hat{\sigma}_{xy}(x,0^{\pm}) - m(x)[\sigma_{xx}^{(0)}(x,0^{\pm}) \\ & - \sigma_{yy}^{(0)}(x,0^{\pm})] + h(x)\frac{\partial\sigma_{xy}^{(0)}}{\partial y}\bigg|_{y=0^{\pm}},\end{aligned} \tag{A13}$$

$$\begin{aligned}\sigma^{\pm}(x) = {} & -\sigma_{yy}^{(0)}(x,0^{\pm}) - \hat{\sigma}_{yy}(x,0^{\pm}) + 2m(x)\sigma_{xy}^{(0)}(x,0^{\pm}) \\ & - h(x)\frac{\partial\sigma_{yy}^{(0)}}{\partial y}\bigg|_{y=0^{\pm}}.\end{aligned} \tag{A14}$$

We will also need to calculate the Fourier transform of the fields on the fault:

$$\begin{aligned}U_i^{\pm}(k) &= \int_{-\infty}^{\infty} u_i(x,0^{\pm})e^{-ikx}dx \quad \text{and} \\ \Sigma_{ij}^{\pm}(k) &= \int_{-\infty}^{\infty} \sigma_{ij}(x,0^{\pm})e^{-ikx}dx.\end{aligned} \tag{A15}$$

Elasticity relates the transforms of stress and displacement (e.g., Geubelle and Rice, 1995):

$$\Sigma_{xx}^{\pm}(k)/G = ik\frac{2(3-2\nu)}{3-4\nu}U_x^{\pm}(k) \mp |k|\frac{4\nu}{3-4\nu}U_y^{\pm}(k), \tag{A16}$$

$$\Sigma_{xy}^{\pm}(k)/G = \mp|k|\frac{4(1-\nu)}{3-4\nu}U_x^{\pm}(k) + ik\frac{2(1-2\nu)}{3-4\nu}U_y^{\pm}(k), \tag{A17}$$

$$\Sigma_{yy}^{\pm}(k)/G = -ik\frac{2(1-2\nu)}{3-4\nu}U_x^{\pm}(k) \mp |k|\frac{4(1-\nu)}{3-4\nu}U_y^{\pm}(k). \tag{A18}$$

The Fourier coefficients are to be determined by the boundary conditions.

Quasi-Static Frictional Slip on Nonplanar Faults

Consider the problem of quasi-static slip at constant friction f with no opening in a prestressed medium. Along with continuity of the traction components of stress, $\tau^+(x) = \tau^-(x)$ and $\sigma^+(x) = \sigma^-(x)$, the boundary conditions are

$$\omega(x) = 0 \quad \text{and} \quad \tau(x) = f\sigma(x). \tag{A19}$$

The solution for a flat fault (the zeroth-order solution) with uniform slip Δu is

$$\begin{aligned}u_x^{(0)}(x,y) &= \frac{\Delta u}{2}\text{sgn}(y), \\ u_y^{(0)}(x,y) &= 0, \\ \sigma_{xx}^{(0)}(x,y) &= \sigma_{xx}^0,\end{aligned} \tag{A20}$$

$$\begin{aligned}\sigma_{xy}^{(0)}(x,y) &= \sigma_{xy}^0 = -f\sigma_{yy}^0, \\ \sigma_{yy}^{(0)}(x,y) &= \sigma_{yy}^0.\end{aligned} \tag{A21}$$

(Terms that are linear in x and/or y can be added to the displacements in order to be compatible with the prestress state. However, such terms would play no role in the analysis to follow and are not explicitly written.) The fields on the fault for the perturbed problem, given in equations (A11)–(A14), simplify with this zeroth-order solution:

$$\delta(x) = \Delta u + \hat{u}_x(x,0^+) - \hat{u}_x(x,0^-), \tag{A22}$$

$$\omega(x) = \hat{u}_y(x,0^+) - \hat{u}_y(x,0^-) - m(x)\Delta u, \tag{A23}$$

$$\tau^{\pm}(x) = \sigma_{xy}^0 + \hat{\sigma}_{xy}(x,0^{\pm}) - m(x)(\sigma_{xx}^0 - \sigma_{yy}^0), \tag{A24}$$

$$\sigma^{\pm}(x) = -\sigma_{yy}^0 - \hat{\sigma}_{yy}(x,0^{\pm}) + 2m(x)\sigma_{xy}^0. \tag{A25}$$

To satisfy the boundary conditions to $O(\epsilon)$, the following conditions must hold:

$$\hat{\sigma}_{xy}(x,0^+) - \hat{\sigma}_{xy}(x,0^-) = 0, \tag{A26}$$

$$\hat{\sigma}_{yy}(x,0^+) - \hat{\sigma}_{yy}(x,0^-) = 0, \tag{A27}$$

$$\hat{u}_y(x,0^+) - \hat{u}_y(x,0^-) = m(x)\Delta u, \tag{A28}$$

$$\hat{\sigma}_{xy}(x,0) + f\hat{\sigma}_{yy}(x,0) = m(x)(\sigma^0_{xx} - \sigma^0_{yy} + 2f\sigma^0_{xy}). \tag{A29}$$

These expressions, which involve fields from the zeroth-order solution on the right-hand side, constitute the boundary conditions on the first-order field perturbations on the left-hand side. By Fourier transforming these expressions and using the elasticity relations of equations (A16)–(A18), we find

$$\hat{U}^+_x(k) - \hat{U}^-_x(k) = -fM(k)\Delta u - \frac{2(1-\nu)}{G|k|}M(k) \times (\sigma^0_{xx} - \sigma^0_{yy} + 2f\sigma^0_{xy}), \tag{A30}$$

$$\hat{\Sigma}_{yy}(k) = -\frac{G\Delta u}{2(1-\nu)}|k|M(k), \tag{A31}$$

$$\hat{\Sigma}_{xy}(k) = -f\hat{\Sigma}_{yy}(k) + M(k)(\sigma^0_{xx} - \sigma^0_{yy} + 2f\sigma^0_{xy}), \tag{A32}$$

$$\hat{\Sigma}^{\pm}_{xx}(k) = -\frac{G\Delta u}{2(1-\nu)}(|k| \pm 2ikf)M(k) \pm 2|k|H(k) \times (\sigma^0_{xx} - \sigma^0_{yy} + 2f\sigma^0_{xy}), \tag{A33}$$

where $M(k) = ikH(k)$ is the transform of the slope, $m(x)$. The first terms, proportional to Δu, are the most relevant. They represent the perturbations due to slip; the other terms are simply the result of projecting the uniform prestress field onto the nonplanar fault surface.

We can invert these transforms using the convolution theorem to obtain

$$\hat{u}_x(x,0^+) - \hat{u}_x(x,0^-) = -fm(x)\Delta u + \frac{2(1-\nu)}{G}\mathcal{H}[h(x)] \times (\sigma^0_{xx} - \sigma^0_{yy} + 2f\sigma^0_{xy}), \tag{A34}$$

$$\hat{\sigma}_{yy}(x,0) = -\frac{G\Delta u}{2(1-\nu)}\mathcal{H}[m'(x)], \tag{A35}$$

$$\hat{\sigma}_{xy}(x,0) = -f\hat{\sigma}_{yy}(x,0) + m(x)(\sigma^0_{xx} - \sigma^0_{yy} + 2f\sigma^0_{xy}), \tag{A36}$$

$$\hat{\sigma}_{xx}(x,0^{\pm}) = -\frac{G\Delta u}{2(1-\nu)}\{\mathcal{H}[m'(x)] \pm 2fm'(x)\} \pm 2\mathcal{H}[m(x)] \times (\sigma^0_{xx} - \sigma^0_{yy} + 2f\sigma^0_{xy}), \tag{A37}$$

where the Hilbert transform of some function $g(x)$ is

$$\mathcal{H}[g(x)] = \frac{1}{\pi}\int_{-\infty}^{\infty}\frac{g(\xi)}{x-\xi}d\xi. \tag{A38}$$

Power Spectral Density of Normal Stress Perturbations on Fractal Faults

Next we relate the power spectral density of normal stress perturbations on the fault, $P_\sigma(k)$, to that of the profile itself. We do this by first relating the autocorrelation of the stress perturbations, $R_\sigma(x)$, to that of the profile, $R_h(x)$:

$$\begin{aligned} R_\sigma(x) &= \lim_{L\to\infty}\frac{1}{L}\int_{-L/2}^{L/2}\hat{\sigma}_{yy}(\xi,0)\hat{\sigma}_{yy}(\xi+x,0)d\xi \\ &= \left[\frac{G\Delta u}{2(1-\nu)}\right]^2\lim_{L\to\infty}\frac{1}{L}\int_{-L/2}^{L/2}\mathcal{H}[m'(\xi)]\mathcal{H}[m'(\xi+x)]d\xi \\ &= \left[\frac{G\Delta u}{2(1-\nu)}\right]^2\lim_{L\to\infty}\frac{1}{L}\int_{-L/2}^{L/2}m'(\xi)m'(\xi+x)d\xi \\ &= \left[\frac{G\Delta u}{2(1-\nu)}\right]^2\frac{d^4}{dx^4}\lim_{L\to\infty}\frac{1}{L}\int_{-L/2}^{L/2}h(\xi)h(\xi+x)d\xi \\ &= \left[\frac{G\Delta u}{2(1-\nu)}\right]^2\frac{d^4}{dx^4}R_h(x). \end{aligned} \tag{A39}$$

In this derivation, we first used equation (A35) to relate the stress perturbations to the fault profile. We then utilized the fact that the autocorrelation of a function is identical to that of its Hilbert transform, and the relation between the autocorrelation of a function's derivative and that of the function itself. Fourier transforming both sides yields

$$P_\sigma(k) = \left[\frac{G\Delta u}{2(1-\nu)}\right]^2 k^4 P_h(k). \tag{A40}$$

A more direct route to this expression is to rewrite equation (A31) as $\hat{\Sigma}_{yy}(k) = T(k)H(k)$, where $T(k) = -ik|k|G\Delta u/[2(1-\nu)]$ is the transfer function between input $H(k)$ and output $\hat{\Sigma}_{yy}(k)$; a well-known result from random vibration theory (Newland, 1993, Ch. 7) states that $P_\sigma(k) = |T(k)|^2 P_h(k)$.

For the power law spectral density in equation (6),

$$P_\sigma(k) = \left[\frac{G\Delta u}{2(1-\nu)}\right]^2 C_h|k|^{4-\beta}, \tag{A41}$$

which simplifies for a self-similar fault ($\beta = 3$) to

$$P_\sigma(k) = 2\pi\left(\frac{\pi\alpha G\Delta u}{1-\nu}\right)^2|k|. \tag{A42}$$

The rms normal stress perturbation from wavenumbers between $k_{\min}$ and $k_{\max}$ is

$$\Delta\sigma_{\mathrm{rms}}(k_{\mathrm{min}}, k_{\mathrm{max}}) = \sqrt{\frac{1}{\pi}\int_{k_{\mathrm{min}}}^{k_{\mathrm{max}}} P_{\sigma}(k)dk}. \qquad \text{(A43)}$$

Unlike the rms roughness, which is determined by the longest wavelengths, the rms normal stress perturbation is dominated by the shortest wavelengths. This is illustrated by considering wavenumbers between $k_{\mathrm{min}} = 0$ and $k_{\mathrm{max}} = 2\pi/\lambda_{\mathrm{min}}$ for the case of a self-similar fault:

$$\Delta\sigma_{\mathrm{rms}}(0, 2\pi/\lambda_{\mathrm{min}}) = 2\pi^2\alpha\frac{G}{1-\nu}\frac{\Delta u}{\lambda_{\mathrm{min}}}. \qquad \text{(A44)}$$

Department of Geophysics
Stanford University
397 Panama Mall
Stanford, California 94305
edunham@stanford.edu
jkozdon@stanford.edu
(E.M.D., J.E.K.)

BBN Technologies
10 Moulton Street
Cambridge, Massachusetts 02138
dbelange@bbn.com
(D.B.)

Stanford Graduate School of Business
518 Memorial Way
Stanford, California 94305
wtsung@stanford.edu
(L.C.)

Manuscript received 24 March 2010